Journal of Materials Chemistry A

Accepted Manuscript

This is an *Accepted Manuscript*, which has been through the Royal Society of Chemistry peer review process and has been accepted for publication.

Accepted Manuscripts are published online shortly after acceptance, before technical editing, formatting and proof reading. Using this free service, authors can make their results available to the community, in citable form, before we publish the edited article. We will replace this *Accepted Manuscript* with the edited and formatted *Advance Article* as soon as it is available.

You can find more information about *Accepted Manuscripts* in the Information for Authors.

Please note that technical editing may introduce minor changes to the text and/or graphics, which may alter content. The journal's standard Terms & Conditions and the Ethical guidelines still apply. In no event shall the Royal Society of Chemistry be held responsible for any errors or omissions in this *Accepted Manuscript* or any consequences arising from the use of any information it contains.

ROYAL SOCIETY OF CHEMISTRY

www.rsc.org/materialsA

Low-Cost High-Performance Asymmetric Supercapacitors Based on Co_2AlO_4@MnO_2 Nanosheets and Fe_3O_4 Nanoflakes

Fei Li[a], *Hao Chen*[a], *Xiao Ying Liu*[a], *Shi Jin Zhu*[a], *Jia Qi Jia*[a], *Chao He Xu*[b]*, *Fan Dong*[c], *Zhong Quan Wen*[d], *Yu Xin Zhang*[a,d]*

[a]College of Material Science and Engineering, Chongqing University, Chongqing 400044, P.R. China

[b]College of Aerospace Engineering, Chongqing University, Chongqing 400044, P.R. China

[c]Chongqing Key Laboratory of Catalysis and Functional Organic Molecules, College of Environmental and Biological Engineering, Chongqing Technology and Business University, 400067 Chongqing, P.R. China

[d]National Key Laboratory of Fundamental Science of Micro/Nano-Devices and System Technology, Chongqing University, Chongqing, 400044, P.R. China

*E-mail: zhangyuxin@cqu.edu.cn ; xche@cqu.edu.cn

Fax: +86-23 6510 4131; TEL: +86-23 6510 4131

Abstract

The development of portable and wearable electronics has promoted increasing demand for high-performance power sources with high energy/power density, low cost, lightweight, as well as ultrathin and flexible features. Herein, a low-cost high-performance flexible asymmetric supercapacitor (ASC) with Co_2AlO_4@MnO_2 nanosheets and Fe_3O_4 nanoflakes grown on nickel foam is designed and fabricated. The as-designed ASC device with an extended operating voltage window of 1.6 V achieves a specific capacitance of 99.1 F g^{-1} at a current density of 2 A g^{-1} with a maximum energy density of 35.3 Wh kg^{-1} and a very long-term cycling stability (92.4% capacitance after 5000 cycles).

Keywords: MnO_2; Co_2AlO_4; Fe_3O_4 Nanoflakes; Supercapacitor.

Introduction

The large proliferation of consumer electronics generally requires high-energy-density and

Journal of Materials Chemistry A Accepted Manuscript

long-lasting power sources[1-3]. Among the various energy storage technologies, super-capacitors (SCs) have emerged as a promising candidate to satisfy increasing power demands in view of the advantages of higher power densities, faster charge-discharge rates and better cyclic stabilities than batteries, and higher energy densities than conventional dielectric capacitors[4-6]. However, the energy density (E) is usually limited to the operating voltage (V) according to the equation $E=1/2CV^2$, where C is the device capacitance. Recently, designing asymmetric supercapacitors (ASCs) has been an effective approach to provide effective power sources due to their potentially broader operating voltage windows and larger capacitances, which can meet the demands of emerging technologies[7, 8]. According to the mechanism of charge storage, SCs can be classified into two kinds: electrical double-layer capacitances (EDLCs), whose charges are adsorbed electrostatically at the electrode/electrolyte interface, typically based on carbon materials; pseudocapacitances, which store energy by redox reactions on electrode materials, usually based on conducting polymers and transition metal oxides[9-12]. In fact, pseudocapacitors have higher specific capacitance than conventional EDLCs due to their fast and reversible redox reaction, so many efforts, have been focused on further improving pseudocapacitors[13, 14].

Up to now, transition metal oxides such as MnO_2[15], Fe_3O_4[16], Fe_2O_3[17], Co_3O_4[18], NiO[19], CuO[20] and V_2O_5[21], none the less dominate the landscape of active materials for electrochemical energy storage. MnO_2 has significant predominance when used as a electrode for SCs such as low cost, abundant resource, and high theoretical specific capacitance (1370 F g^{-1})[22, 23]. However, most MnO_2-based materials exhibit poor electrical conductivity, volume expansion and severe aggregation during the redox reactions, which could lead to the inadequate utilization and pulverization of the active materials. An effective approach is the design of heterostructure with the combination of metal composite oxide and different crystalline phases MnO_2 such as $ZnCo_2O_4$@MnO_2[24], $NiCo_2O_4$@MnO_2[25] and $MnCo_2O_{4.5}$@MnO_2[26]. The coupling of different metal species could render the core–shell composite with rich redox reactions which are beneficial to electrochemical applications. However, to date, little study was done by rationally combining the merits of Co_2AlO_4 and MnO_2 for SCs. On the other hand, Fe_3O_4 can be considered as a promising candidate of anode electrode for SCs owing to its abundance, low cost, and environmental friendliness[27, 28]. However, the experimentally observed capacitance of Fe_3O_4 is considerably lower than the expected value. Its cycling performance is very poor due to the possible dissolution of Fe during the charge and discharge processes[29]. And the agglomeration of bulk Fe_3O_4 hinders its stable performance. An emerging new concept is to grow electroactive nanostructures

Journal of Materials Chemistry A Accepted Manuscript

on conductive substrates to be directly used as binder-free electrodes for SCs. Therefore, ASC combined with Co_2AlO_4@MnO_2 as cathode and Fe_3O_4 as anode will become a promising energy storage technology that possesses more economical and environmental superiority.

Herein, we demonstrate a facile and cost-effective approach to design and fabricate hierarchical Co_2AlO_4@MnO_2 nanocomposites arrays on nickel foam for high-performance SCs. Due to the favorable nanostructure, it exhibits an improved specific capacitance of 915.1 F g^{-1} at 2 A g^{-1}, making it a perfect cathode candidate to match with the Fe_3O_4 nanoflakes anode (379.8 F g^{-1} at 2 A g^{-1}). The as-designed ASC device with an extended operating voltage window of 1.6 V achieved a specific capacitance of 99.1 F g^{-1} at a current density of 2 A g^{-1} with a maximum energy density of 35.3 Wh kg^{-1} and a very long-term cycling stability (92.4% capacitance after 5000 cycles).

Experimental

Synthesis of Fe_3O_4 Nanosheet Arrays.

All the reagents were of analytical-reagent grade, and used without further purification. In a typical synthesis, $Fe(NO_3)_3$•$9H_2O$ (1 mmol), NH_4F (1 mmol), $CO(NH_2)_2$ (5 mmol) were dissolved in 30 mL of deionized water and stirred for 10 min to form a clear solution. Nickel foam (1× 1.5 cm^2) was carefully cleaned with 3 M HCl solution in an ultrasound bath for 5 min to remove the surface NiO layer, and then cleaned with deionized water and ethanol for 5 min each. The aqueous solution and the Ni foam were transferred to a Teflon-lined stainless-steel autoclave and maintained at 120 ^oC for 6 h, and then cooled down to room temperature. The samples were rinsed several times with deionized water and ethanol with the assistance of ultrasonication, and dried at 80 ^oC for 8 h. Finally, the precursors were converted to Fe_3O_4 by annealing at 350 ^oC for 2 h.

Synthesis of Co_2AlO_4 Nanosheet Arrays.

In a typical synthesis, $Al(NO_3)_3$•$6H_2O$ (1 mmol), $Co(NO_3)_2$•$6H_2O$ (2 mmol), NH_4F (1 mmol), $CO(NH_2)_2$ (5 mmol) were dissolved in 30 mL of deionized water and stirred for 10 min to form a clear solution. Nickel foam (1× 1.5 cm^2) was carefully cleaned with 3 M HCl solution in an ultrasound bath for 5 min to remove the surface NiO layer, and then cleaned with deionized water and ethanol for 5 min each. The aqueous solution and the Ni foam were transferred to a Teflon-lined stainless-steel autoclave and maintained at 90 ^oC for 6 h, and then cooled down to room temperature. The samples were rinsed several times with deionized water and ethanol with the assistance of ultrasonication, and dried at 80 ^oC for 8 h. Finally, the precursors were converted to Co_2AlO_4 by annealing at 350 ^oC for 2 h.

Journal of Materials Chemistry A Accepted Manuscript

Synthesis of Co_2AlO_4@MnO_2 Nanosheet Arrays.

The hierarchical Co_2AlO_4@MnO_2 arrays were prepared using a facile hydrothermal method. Typically, the Co_2AlO_4 nanosheets arrays on Ni foam was put into a Teflon-line stainless steel autoclave containing 30 mL $KMnO_4$ solution (0.01 M), which was subsequently maintained at 160 ^oC for 24 h. Finally, the samples were removed, washed with deionized water and ethanol, and dried at 60 ^oC to obtain hierarchical Co_2AlO_4@MnO_2 arrays. The mass of the as-grown MnO_2 materials was obtained by its weight differences before and after hydrothermal deposition.

Assembly of Asymmetric NF-Co_2AlO_4@MnO_2 // NF-Fe_3O_4 SCs Device.

The ASC were assembled by using NF-Co_2AlO_4@MnO_2 as cathode electrode and NF-Fe_3O_4 as anode electrode with a separator. The NF-Co_2AlO_4@MnO_2// NF-Fe_3O_4 SC device (area: 1 cm × 1.5 cm, the total weight of the electrode materials: 4.2 mg exclude the nickel foam) was fabricated by assembly of a PVA–KOH solid electrolyte membrane between the NF-Co_2AlO_4@MnO_2 (cathode electrode) and the NF-Fe_3O_4 (anode electrode) face-to-face. After hot pressing at 60 °C for 5 min, the electrolyte was solidified to produce a sandwich structure. The overall thickness of this all-solid-state EC is≈0.3 mm, facilitating a close contact between the electrolyte and electrode.

Materials characterizations.

The crystallographic information and chemical composition of as-prepared products were established by powder X-ray diffraction (XRD, D/max 1200, Cu Kα). The morphological investigations of the products were carried out with focused ion beam (Zeiss Auriga FIB/SEM) and transmission electron microscopy (TEM, ZEISS LIBRA 200). Nitrogen adsorption-desorption isotherms were measured at 77 K with micrometritics ASAP 2020 sorptometer. The specific surface area was calculated with the Brunauer-Emmett-Teller (BET) equation, and the pore size distributions were calculated from the adsorption curve by the Barrett–Joyner–Halenda (BJH) method.

Electrochemical Measurements.

The electrochemical properties of the electrodes were carried out using an electrochemical workstation (CHI 660E) with three-electrode configuration in a 2 M KOH aqueous solution. The Fe_3O_4, Co_2AlO_4 and Co_2AlO_4@MnO_2 on Ni foam were directly used as the working electrode. Platinum plate was used as the counter electrode and saturated calomel electrode (SCE) as the reference electrode, respectively.

The specific capacitance of the samples was calculated from the charge–discharge curves based on the following equation[30, 31]:

Journal of Materials Chemistry A Accepted Manuscript

$$C = \frac{I \times \Delta t}{m \times \Delta V} \quad (1)$$

where m, I, Δt and ΔV are the weight (g) of the electroactive materials, discharge current (A), the discharging time (s), and the discharging potential range (V), respectively.

Energy density and power density of the flexible EC device were calculated using the following equations:

$$Ct = \frac{I \times \Delta t}{m_t \times \Delta V} \quad (2)$$

$$E = \frac{C \times \Delta V^2}{2} \quad (3)$$

$$P = \frac{E}{\Delta t} \quad (4)$$

where Ct (F g^{-1}) is the capacitance of EC device; I (A) represents the discharge current; ΔV (V) refers to the potential change within the discharge time Δ t (s); m_t (g) is the total weight of the electrode materials of EC device; E (Wh kg^{-1}) and P (kW kg^{-1}) correspond to the energy density and power density, respectively.

Results and discussion

The growth procedures of Co_2AlO_4@MnO_2 and Fe_3O_4 nanosheets on nickel foam and the design of ASC are schematically illustrated in Fig. 1. The rechargeable ASC are constructed by direct growth of Co_2AlO_4@MnO_2 nanosheets (cathode material) and Fe_3O_4 nanosheets (anode material) on the NF. The novel flexible ASC demonstrate superior energy and power densities stemming from the nanosized feature of active materials and the hierarchical structure of the electrodes.

The SEM data (Fig. 2a and in set of Fig. 2a) reveals that the Fe_3O_4 nanosheets grow vertically and are cross-linked on the Ni substrate and the array consists of regular hexagonal nanosheets, typically 0.5–1 μm in length and 30–50 nm in thickness, arranged as a dense film on the nickel foam. And the TEM image in Fig. 2b shows that the Fe_3O_4 nanoflakes are composed of numerous nanoparticles and nanopores. Well-resolved lattice spacings observed from the HRTEM images (Fig. 2c) correspond to a d-spacing value of 0.24 nm, consistent with the (222) planes of a magnetite-Fe_3O_4. The corresponding diffraction rings of (111), (311) and (440) in the selected area electron diffraction (SAED) patterns (Fig. 2d) confirm the formation of magnetite-Fe_3O_4[32, 33]. The structure of the Fe_3O_4/NF composite is also

Journal of Materials Chemistry A Accepted Manuscript

studied by EDS mapping (Fig. 2e). The elemental maps of O and Fe show a uniform and continuous dispersion throughout the nickel foam network, indicating a continuous Fe_3O_4 film was formed on the NF surface. XRD pattern in Fig. 2f is employed to investigate the crystalline structures and phase purity of the as-prepared Fe_3O_4/NF composite and pure Fe_3O_4 (some Fe_3O_4 particles are observed in the solution from the same reaction batch that are not attached to the NF, and they, also composed of nanoflakes, are roughly spherical with a diameter of about 2-3 μm, Fig. S1). All of the reflections of Fe_3O_4 are consistent with the patterns reported for the Fe_3O_4 (JCPDS card no. 75-0449). The diffraction peaks at 2θ = 35.76, 37.41, 43.47 and 63.17^o can be indexed to the (311), (222), (400) and (440) reflections, respectively. The sharp and narrow diffraction peaks indicate that the Fe_3O_4 microstructures have high crystallinity. Furthermore, except for the peaks originating from the Ni foam, the diffraction peaks of Fe_3O_4 in the pattern of Fe_3O_4/NF composite are observed, which are coincided with the curve of pure Fe_3O_4.

Fig. 3a and b show the scanning electron microscopy (SEM) images of Co_2AlO_4 nanosheets on NF. The Co_2AlO_4 nanosheets grow vertically and are cross-linked on the Ni substrate, which are similar to the Fe_3O_4 nanosheets. However, the length and thickness of the Co_2AlO_4 nanosheets have some expansion, to about 1–2 μm and 50–80 nm, respectively. Fig. 3c presents the composition and crystallite phase purity of the Co_2AlO_4 nanosheets on NF. Except for the peaks originating from the Ni foam, the diffraction peaks are observed of 18.99, 31.25, 36.82 and 65.22^o, which could be assigned to the (111) (220), (311) and (440) planes of Co_2AlO_4 (JCPDS 38-0814), respectively[34, 35]. TEM images collected from Co_2AlO_4 nanostructure also verify its nanosheet morphology, and the SAED pattern indicates that the Co_2AlO_4 nanosheets are polycrystalline. Well-resolved lattice fringes of 0.234 nm is observed, corresponding to the (222) plane of Co_2AlO_4 (JCPDS 38-0814). And EDS mapping of the Co_2AlO_4 nanosheets are shown in Fig. 3g. The elemental maps of O, Al, Co and Ni show a uniform and continuous dispersion throughout the nickel foam network, indicating a continuous Co_2AlO_4 film is formed on the NF surface.

We can found from Fig. 4a and b that the cross-linked MnO_2 nanosheets are clearly observed on the surface of Co_2AlO_4 nanoflakes, which provide abundant interstitial space in the composite. This unique structure can not only supply sufficient electrochemically active sites on the surface of MnO_2, but increase the effective liquid–solid interfacial area, provide a fast path for the insertion and extraction of electrolyte ions, and consequently facilitate the Faraday reaction. As shown in XRD

Journal of Materials Chemistry A Accepted Manuscript

pattern of NF-Co_2AlO_4@MnO_2, except for the peaks originating from the Ni foam and Co_2AlO_4, the diffraction peaks of MnO_2 nanosheets are observed of 12.5° and 25.2°, which could be assigned to the (001) and (002) planes of birnessite-type MnO_2 (JCPDS 80-1098)[36, 37]. The detailed structural information of Co_2AlO_4@MnO_2 is further provided by TEM (Fig. 4d), which indicate that the Co_2AlO_4 nanoflakes are uniformly covered with small MnO_2 nanosheets. HRTEM image (Fig. 4e) of the MnO_2 nanosheets reveals well-resolved lattice fringe having an interplanar spacing of 0.227 nm, which is well consistent with the distance of the (111) plane of birnessite-type MnO_2. The selected area electron diffraction (SAED) pattern demonstrates that the MnO_2 nanosheets have a polycrystalline structure, and the three diffraction rings are corresponded to the (001) (110) and (113) crystal planes of MnO_2, respectively, in agreement with the XRD results. The elemental maps of O, Al, Co, Ni and Mn in Fig. 4g show a uniform and continuous dispersion throughout the nickel foam network, indicating the Co_2AlO_4 nanoflakes are uniformly covered with small MnO_2 nanosheets.

As reported, active materials with large surface area which can increase the active sites for getting electrons or for Faradaic reactions have been applied to improve the performance for SCs. Therefore, the N_2 adsorption-desorption isotherms and the Barrett-Joyner-Halenda (BJH) pore size distribution curves (inset) of the three samples (The BET samples are prepared by scratching the Fe_3O_4, Co_2AlO_4, Co_2AlO_4@MnO_2 from Ni foam) are presented in Fig. 5. It can be seen that all the isotherms of the three samples belong to type IV according to IUPAC classification, indicating the presence of mesopores derived from the self-assembly of 2D nanosheet building blocks. Because of the porous structure, the porous Fe_3O_4, Co_2AlO_4, and Co_2AlO_4@MnO_2 exhibit large surface area of 137.8, 99.7 and 205.9 $m^2 g^{-1}$, respectively. The large increase in surface area after the deposition of MnO_2 arises from the meso/microporosity of the coating. The BJH pore size distributions calculated from the desorption data indicate that the average pore diameter of Co_2AlO_4@MnO_2 pattern is about 9.81 nm. On the other hand, the average pore diameters of Fe_3O_4 pattern and Co_2AlO_4 pattern are 11.33 nm and 13.15 nm, respectively. The large surface area is favorable for enhancing the electrolyte material contact area and providing large reactive reaction area. Such types of hierarchical surface morphologies with well developed pore structures are advantageous for enhancive electro-chemical capacitors applications.

The above material characterization reveals that the nanosheets had meso/macropore and a large surface area, making them an ideal choice for electrodes in SCs. The electrochemical properties of NF-Co_2AlO_4@MnO_2 (NF-Co_2AlO_4) cathode and NF-Fe_3O_4 anode are investigated in a three-electrode

Journal of Materials Chemistry A Accepted Manuscript

configuration containing 2 M KOH solution. Fig. 6a depicts the cyclic voltammetric (CV) curves of the NF-Fe_3O_4, NF-Co_2AlO_4 and NF-Co_2AlO_4@MnO_2 electrodes, respectively. Apparently, a pair of redox peaks is observed for the Co_2AlO_4 nanosheet arrays electrode, which corresponds to the reversible reaction of the $Co^{2+}/Co^{3+}$and Co^{3+}/Co^{4+}associated with OH^-. Remarkably, a similar CV shape is still found for the Co_2AlO_4@MnO_2 core–shell nanosheet arrays, indicating the efficient utilization of the underlying Co_2AlO_4 nanosheets despite covered by the MnO_2 nanoflakes, while the area integrated within the current–potential curves greatly increases for the core–shell nanosheet arrays, leading to a much larger pseudocapacitance. It should be attributed to the additional pseudocapacitance contributed by the MnO_2 shell, which can adsorb K^+ cations on the electrode surface and/or possibly intercalate and deintercalate K^+ ions. On the other hand, the Fe_3O_4 CV curves exhibit an osteosclerosisand shape that was an indicative of pseudocapacitive behavior. The pseudocapacitance of Fe_3O_4 might arise from a reversible Fe^{3+}/Fe^{2+} couple. Based upon the above experimental results and discussion, the perfect matching between NF-Co_2AlO_4@MnO_2 (NF-Co_2AlO_4) and NF-Fe_3O_4 are quite obvious. They exhibit large pseudocapacitance in the exactly complementary potential windows. Thus, the Co_2AlO_4@MnO_2 and Fe_3O_4 nanosheets on NF can be used as cathodes and anodes to assemble asymmetric NF-Co_2AlO_4@MnO_2 // NF-Fe_3O_4 ASC device.

Fig. 6b shows the galvanostatic charge-discharge curves of the three electrodes within a potential range of 0－0.4 V for NF-Co_2AlO_4@MnO_2 (NF-Co_2AlO_4) and -1－0 V for NF-Fe_3O_4, from which the corresponding specific capacitance are estimated to be 379.8, 575.2, and 915.1 F g^{-1} at the current density of 2 A g^{-1} for the NF-Fe_3O_4, NF-Co_2AlO_4 and NF-Co_2AlO_4@MnO_2 electrodes, respectively. Even at a high current density of 10 A g^{-1}, they still retain a specific capacitance of 272.2, 403 and 694 F g^{-1}, respectively, showing excellent rate performance (Fig. 6c). The outstanding rate capability could be attributed to the remarkable conductivity of the NF substrate. Furthermore, the capacitance reported here is much higher than those of previously reported directly-grown pseudo-capacitive array nanoarchitectures[13,19,37].

Fig. 6d shows Nyquist plots of the NF-Fe_3O_4, NF-Co_2AlO_4 and NF-Co_2AlO_4@MnO_2 electrodes, which are measured in a frequency range of 100 kHz to 0.1 Hz. The corresponding equivalent circuit consists of a series and parallel combination of resistances, Rs (contributions of ionic resistance of electrolyte, intrinsic resistance, and contact resistance between active material and current collector), Rct (charge transfer resistance), CPE (constant phase element), and W (Warburg impedance). Through

Journal of Materials Chemistry A Accepted Manuscript

a fitting analysis, the related Rct of the NF-Fe_3O_4, NF-Co_2AlO_4 and NF-Co_2AlO_4@MnO_2 electrode have low value of 1.5, 0.6 and 0.22 Ω. The Rs of the NF-Fe_3O_4, NF-Co_2AlO_4 and NF-Co_2AlO_4@MnO_2 electrode are 0.8, 0.8 and 1.3 Ω, which is determined by the point where the semicircle intersects with the Z'-axis. The low values of Rct and Re are mainly attributed to the high specific surface area of porous Fe_3O_4, Co_2AlO_4 and Co_2AlO_4@MnO_2, which facilitates a charge transfer and a faster ion insertion/extraction during electrochemical reactions. The almost vertical line in the low frequency region is indicative of the rapid ion transport that the porosity allows between electrode and electrolyte as well as through the latter.

The long-term cyclic stability of SCs is another critical issue in practical use. The three electrodes are subjected to an extended charge-discharge cycling at 10 A g^{-1}. The result in Fig. 6e presents that the Co_2AlO_4@MnO_2 electrode exhibit an excellent long-term stability with only 3.9% capacitance loss after 2000 cycles, which is much better than 6.7% capacitance loss for the Co_2AlO_4 electrode after the same cycles. Furthermore, 94.32% of the original capacitance was reserved after 2000 cycles for Fe_3O_4, also indicating excellent cycling stability.

Fig. 7a shows the schematic illustration of the full-cell package, where the two electrodes (the Co_2AlO_4@MnO_2 and Fe_3O_4 nanosheets on NF are used as cathodes and anodes) are separated with an electrolyte-soaked separator and packed between two PET films. Fig. S2a shows the CV curves of the device at different voltage windows at a scan rate of 100 mV s^{-1}. As expected, the stable electrochemical windows of the asymmetric supercapacitor device can be extended to 1.6 V. Fig. 7b shows the CV curves of the ASC device at different scan rates within a cell voltage window of 0－1.6 V. A couple of redox peaks are observed, indicating the pesudoreaction from the electrodes (Fe^0－Fe^{3+} and Co^{2+}－Co^{4+}). Galvanostatic charge-discharge tests of the ASC device are conducted (Fig. S2b), and the rate capability is shown in Fig. 7c. Within a short discharge time of 158.6 s, the ASC device can deliver a specific capacitance of 99.1 F/g (based on the mass of the whole electrode materials). When the current density further increases to 10 A/g, at a corresponding discharge time of only 10.8 s, the device could maintain a specific capacitance of 67.8 F/g, showing the desirable rate performance. In addition, the digital images inserted in Fig. 7c shows that our NF-Co_2AlO_4@MnO_2 // NF-Fe_3O_4 ASC device possesses good flexibility. The CV curves under (at current density 50mV/s) bending conditions are collected in the Fig. S3, the shape of the CV curves do not change significantly, even at a bending angle of 180 °. The cycling stability of the ASC device is further investigated by virtue of galvanostatic

Journal of Materials Chemistry A Accepted Manuscript

charge/discharge cycling between 0 and 1.6 V at 5 A g^{-1} (as shown in Fig. 7d). The specific capacitance retained 92.4% after 5000 cycles, indicating its good cycle stability. Furthermore, two SCs are connected in series to light a green light-emitting-diode (LED) that have the lowest operating voltage of 1.8 V, the LED was on for about 120 seconds after being charged for 10.8 s (Fig. 7d inset). These results demonstrate that our device has great electrochemical performance and practical application. Fig. 7e shows the Ragone plots of the NF-Co_2AlO_4@MnO_2 // NF-Fe_3O_4 ASC device based on galvanostatic charge-discharge tests in a voltage window of 0–1.6 V. It is worth noting that the maximum energy density obtained for our asymmetric supercapacitor devices is 35.25 Wh kg^{-1} at a power density of 800.1 W kg^{-1}. Even at a high power density of 8033 W kg^{-1}, the ASC can deliver a high energy density of 24.11 Wh kg^{-1}. The combination of high energy and power densities of the NF-Co_2AlO_4@MnO_2 // NF-Fe_3O_4 full device are compared favorably with previously reported studies[38-43]. Fig. S4 shows Nyquist plots of the NF-Co_2AlO_4@MnO_2 // NF-Fe_3O_4 full device with increasing electrochemical cycles. The internal resistances (Rs) change from 0.9 Ω to 1.1 Ω after 5000 cycles, manifesting a good conductivity of the electrolyte and the very low internal resistance of the electrode. What's more, only a slight increase of the charge transfer resistance (Rct) from 5.6 Ω to 37 Ω is observed after 5000 cycles.

Conclusion

In conclusion, we report the design and successful fabrication of flexible NF-Co_2AlO_4@MnO_2 // NF-Fe_3O_4 ASC device by growing nanostructured active materials, that is, Co_2AlO_4@MnO_2 nanosheets and Fe_3O_4 nanoflakes grown on NF current collectors without any binders or carbon additives. Compared with previously reported ASCs, our newly designed NF-Co_2AlO_4@MnO_2 // NF-Fe_3O_4 ASC device demonstrates excellent stability in a large potential window of 1.6 V and achieves a specific capacitance of 99.13 F g^{-1} at a current density of 2 A g^{-1}. Additionally, our ASC also exhibits excellent energy density of 35.3 Wh kg^{-1} and a very long-term cycling stability (92.4% capacitance after 5000 cycles). The rational design concept for metal oxide nanocomposites can be extended to other metal oxides and some other current collectors, which can pave ways for ultrahigh energy density storage devices.

Supporting information

CV curves at different voltage windows at a scan rate of 100 mV s^{-1}, Galvanostatic charge-discharge tests, The CV curves under different bending conditions and Nyquist plots of the

Journal of Materials Chemistry A Accepted Manuscript

NF-Co_2AlO_4@MnO_2 // NF-Fe_3O_4 full device.

Acknowledgments

The authors gratefully acknowledge the financial supports provided by National Natural Science Foundation of China (Grant no. 51104194 and 21576034), International S &T Cooperation Projects of Chongqing (CSTC2013gjhz90001), National Key laboratory of Fundamental Science of Micro/Nano-device and System Technology (2013MS06, Chongqing University), Laboratory of Precision Manufacturing Technology, CAEP (KF13004), State Education Ministry and Fundamental Research Funds for the Central Universities (Project no. CDJZR14135501, Chongqing University, PR China).

References

1 J.Y. Liao, D. Higgins, G. Lui, V. Chabot, X. Xiao and Z. Chen, *Nano Lett.*, 2013, **13**, 5467-5473.

2 P. H. Yang, X. Xiao, Y. Z. Li, Y. Ding, P. F. Qiang, X. H. Tan, W. J. Mai, Z. Y. Lin, W. Z. Wu, T. Q. Li, H. Y. Jin, P. Y. Liu, J. Zhou, C. P. Wong and Z. L. Wang, *ACS Nano*, 2013, **7**, 2617-2626.

3 A. Banerjee, S. Bhatnagar, K.K. Upadhyay, P. Yadav and S. Ogale, *ACS Appl. Mater. Interfaces*, 2014, **6**, 18844-18852.

4 K. Qiu, Y. Lu, D. Zhang, J. Cheng, H. Yan, J. Xu, X. Liu, J.-K. Kim and Y. Luo, *Nano Energy*, 2015, **11**, 687-696.

5 J. Liu, J. Jiang, C. Cheng, H. Li, J. Zhang, H. Gong and H.J. Fan, *Adv. Mater.*, 2011, **23**, 2076-2081.

6 K. Liang, T. Gu, Z. Cao, X. Tang, W. Hu and B. Wei, *Nano Energy*, 2014, **9**, 245-251.

7 L. H. Du, P. H. Yang, X. Yu, P. Y. Liu, J. H. Song and W. J. Mai, *J. Mater. Chem. A*, 2014, **2**, 17561-17567.

8 G. Lee, D. Kim, D. Kim, S. Oh, J. Yun, J. Kim, S. S. Lee and J. S. Ha, *Energy Environ. Sci.*, 2015, **8**, 1764-1774.

9 W. Chaikittisilp, M. Hu, H. Wang, H.S. Huang, T. Fujita, K.C. Wu, L.C. Chen, Y. Yamauchi and K. Ariga, *Chem. Commun. (Camb)*, 2012, **48**, 7259-7261.

10 Y. Zhu, S. Murali, M.D. Stoller, K.J. Ganesh, W. Cai, P.J. Ferreira, A. Pirkle, R.M. Wallace, K.A. Cychosz, M. Thommes, D. Su, E.A. Stach and R.S. Ruoff, *Science*, 2011, **332**, 1537-1541.

11 Y. Yang, S. Li, L. Zhang, J. Xu, W. Yang and Y. Jiang, *ACS Appl. Mater. Interfaces*, 2013, **5**, 4350-4355.

12 M. Zhi, C. Xiang, J. Li, M. Li and N. Wu, *Nanoscale*, 2013, **5**, 72-88.

13 F. Cao, G.X. Pan, X.H. Xia, P.S. Tang and H.F. Chen, *J. Power Sources*, 2014, **264**, 161-167.

14 Q. Wang, X. Wang, J. Xu, X. Ouyang, X. Hou, D. Chen, R. Wang and G.. Shen, *Nano Energy*, 2014, **8**, 44-51.

15 L. Li, Z.A. Hu, N. An, Y.Y. Yang, Z.M. Li and H.Y. Wu, *J. Phys. Chem. C*, 2014, **118**, 22865-22872.

16 T.W. Lin, C.S. Dai and K.C. Hung, *Sci. Rep.*, 2014, **4**, 7274.

17 K.K. Lee, S. Deng, H.M. Fan, S. Mhaisalkar, H.R. Tan, E.S. Tok, K.P. Loh, W.S. Chin and, C.H. Sow, *Nanoscale*, 2012, **4**, 2958-2961.

18 Y. Xiao, S. Liu, F. Li, A. Zhang, J. Zhao, S. Fang and D. Jia, *Adv. Funct. Mater.*, 2012, **22**, 4052-4059.

Journal of Materials Chemistry A Accepted Manuscript

19 J.B. Wu, R.Q. Guo, X.H. Huang and Y. Lin, *J. Power Sources*, 2013, **243**, 317-322.

20 S.E. Moosavifard, M.F. El-Kady, M.S. Rahmanifar, R.B. Kaner and M.F. Mousavi, *ACS Appl. Mater. Interfaces*, 2015, **7**, 4851-4860.

21 M. Lee, S.K. Balasingam, H.Y. Jeong, W.G. Hong, H.B. Lee, B.H. Kim and Y. Jun, *Sci. Rep.*, 2015, **5**, 8151.

22 W. Wei, X. Cui, W. Chen and D.G. Ivey, *Chem. Soc. Rev.*, 2011, **40**, 1697-1721.

23 L. Peng, X. Peng, B. Liu, C. Wu, Y. Xie and G. Yu, *Nano Lett.*, 2013, **13**, 2151-2157.

24 W. Q. Ma, H. H. Nan, Z. X. Gu, B. Y. Geng and X. J. Zhang, *J. Mater. Chem. A*, *2015*, **3**, 5442 –5454.

25 L. Yu, G. Zhang, C. Yuan and X.W. Lou, *Chem. Commun.(Camb)*, 2013, **49**, 137-139.

26 F. Li, G. Li, H. Chen, J.Q. Jia, F. Dong, Y.B. Hu, Z.G. Shang and Y.X. Zhang, *J. Power Sources*, 2015, **296**, 86-91.

27 W. H. Shi, J. X. Zhu, D. H. Sim, Y. Y. Tay, Z. Y. Lu, X. J. Zhang, Y. Sharma, M. Srinivasan, H. Zhang, H. H. Hng and Q. Y. Yan, *J. Mater. Chem.*, 2011, **21**, 3422–3427.

28 L. Kong, X. Lu, X. Bian, W. Zhang and C. Wang, *ACS Appl. Mater. Interfaces*, 2011, **3**, 35-42.

29 J. Luo, J. Liu, Z. Zeng, C.F. Ng, L. Ma, H. Zhang, J. Lin, Z. Shen and H.J. Fan, *Nano Lett.*, 2013, **13**, 6136-6143.

30 M. Shao, Z. Li, R. Zhang, F. Ning, M. Wei, D.G. Evans and X. Duan, *Small*, 2015.

31 F. Wang, X. Zhan, Z. Cheng, Q. Wang, Z. Wang, F. Wang, K. Xu, Y. Huang, M. Safdar and J. He, *Adv. Electron. Mater.*, 2015, **1**, 1400053.

32 Y.G. Zhu, J. Xie, G.S. Cao, T.J. Zhu and X.B. Zhao, *RSC Adv.*, 2013, **3**, 6787–6793.

33 F.Q. Zhuang, R.Q. Tan, W.F. Shen, X.P. Zhang, W. Xu and W.J. Song, *J. Chem. Eng. Data*, 2014, **59**, 3873-3881.

34 X. P. Wang, J. J. Yu, J. Cheng, Z. P. Hao and Z. P. Xu, *Environ. Sci. Technol.*, 2008, **42**, 614–618.

35 J. Cheng, X. Wang, J. Yu, Z. Hao and Z.P. Xu, *J. Phys. Chem. C*, 2011, **115**, 6651-6660.

36 F. Li, Y. Xing, M. Huang, K. L. Li, T. T. Yu, Y. X. Zhang and D. Losic, *J. Mater. Chem. A*, 2015, **3**, 7855 –7878.

37 M. Huang, X.L. Zhao, F. Li, L.L. Zhang and Y.X. Zhang, *J. Power Sources*, 2015, **277**, 36-43.

38 S. Dai, Y. Xi, C. Hu, X. Yue, L. Cheng and G. Wang, *J. Power Sources*, 2015, **274**, 477-482.

39 D. Sarkar, G.G. Khan, A.K. Singh and K. Mandal, *J. Phys. Chem. C*, 2013, **117**, 15523-15531.

40 D.T. Dam, X. Wang and J.M. Lee, *ACS Appl. Mater. Interfaces*, 2014, **6**, 8246-8256.

41 X. Xia, W. Lei, Q. Hao, W. Wang and X. Wang, *Electrochim. Acta*, 2013, **99**, 253-261.

42 Y.X. Zhang, M. Kuang, X.D. Hao, Y. Liu, M. Huang, X.L. Guo, J. Yan, G.Q. Han and J. Li, *J. Power Sources* **2014,** *270*, 675-683.

43 M. Huang, Y. Zhang, F. Li, L. Zhang, R.S. Ruoff, Z. Wen and Q. Liu, *Sci. Rep.* **2014,** *4*, 3878.

Journal of Materials Chemistry A Accepted Manuscript

Fig. 1. Schematic diagram illustrating the synthesis procedure of $Co_2AlO_4@MnO_2$ and Fe_3O_4 on nickel foam and the designed asymmetric supercapacitor device.

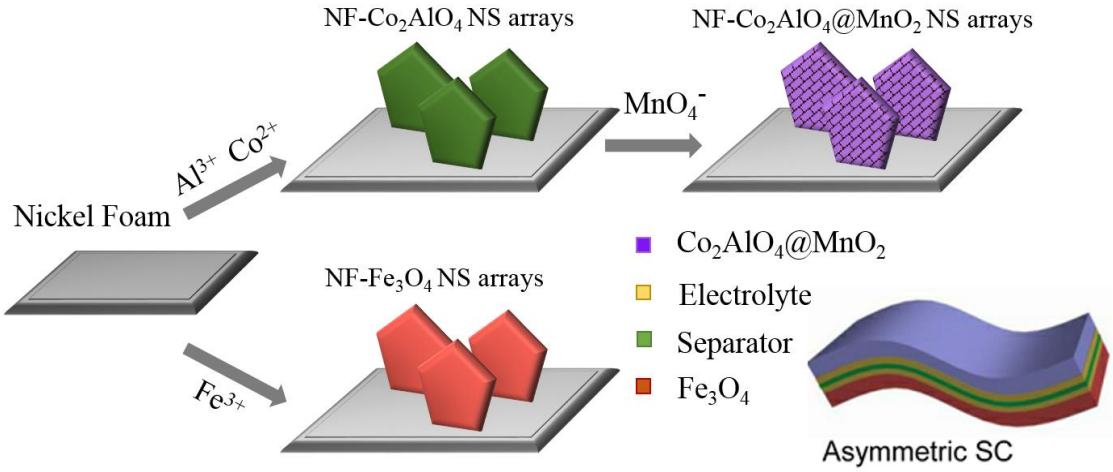

Journal of Materials Chemistry A Accepted Manuscript

Fig. 2. Characterization of the NF-Fe_3O_4. (a) Typical SEM image (inset is magnified SEM image); (b) TEM image and the corresponding HRTEM image(c) and SEAD pattern(d); (e) Element mappings of O, Ni and Fe. (f) XRD patterns.

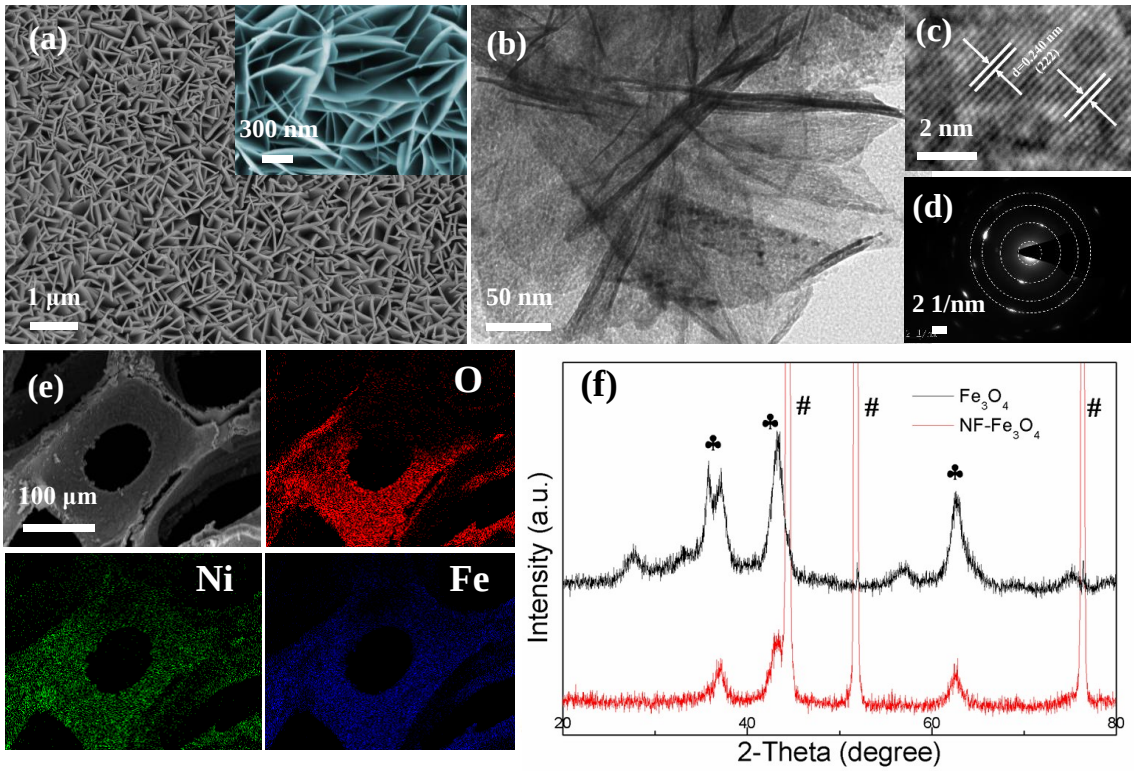

Journal of Materials Chemistry A Accepted Manuscript

Fig. 3. Characterization of the NF-Co_2AlO_4. (a) Typical SEM image and the corresponding magnified SEM image (b); (c) XRD pattern (#:Ni, ♣:Co_2AlO_4); (d) TEM image and the corresponding HRTEM image(e) and SEAD pattern(f); (g) Element mappings of O, Al, Co and Ni.

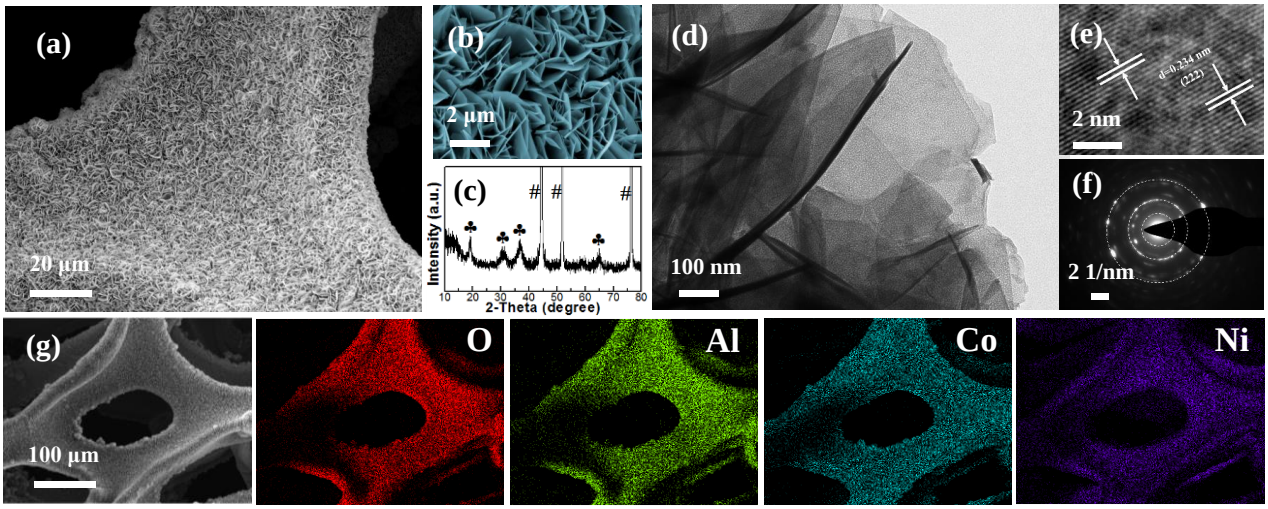

Journal of Materials Chemistry A Accepted Manuscript

Fig. 4. Characterization of the NF-Co_2AlO_4@MnO_2. (a) Typical SEM image and the corresponding magnified SEM image (b); (c) XRD pattern(#:Ni, ♣:Co_2AlO_4, ♥:MnO_2); (d) TEM image and the corresponding HRTEM image(e) and SEAD pattern(f); (g) Element mappings of O, Al, Co and Ni.

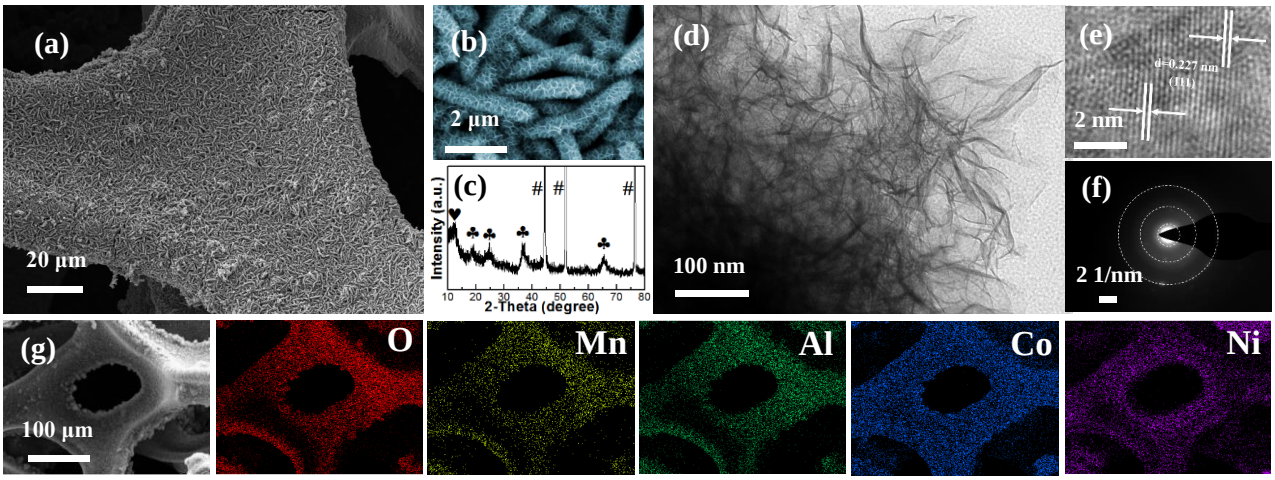

Journal of Materials Chemistry A Accepted Manuscript

Fig. 5. Nitrogen adsorption–desorption isotherms of (a) Fe_3O_4, (b) Co_2AlO_4 and (c) Co_2AlO_4@MnO_2. The insets show the corresponding BJH pore size distributions.

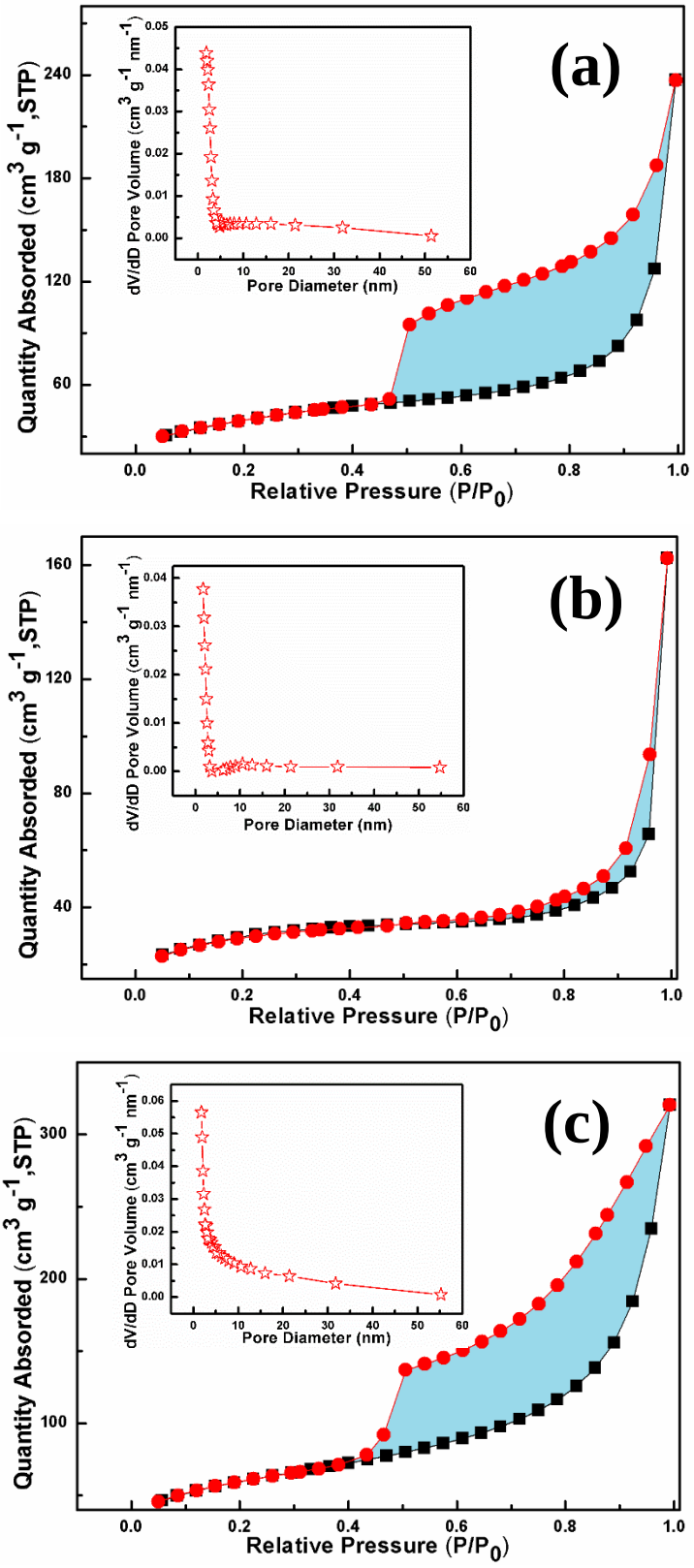

Journal of Materials Chemistry A Accepted Manuscript

Fig. 6. The electrochemical performance of Fe_3O_4, Co_2AlO_4 and Co_2AlO_4@MnO_2 on Ni foam measured in 1 M KOH solution. (a) Cyclic voltammetry curves at 10 mV s^{-1}; (b) Galvanostatic charge–discharge curves at 2A g^{-1}; (c) Specific capacitance under different current densities; (d) Electrochemical impedance spectrum at open circuit potential in the frequency range from 0.01 Hz to 100 kHz; (e) Cycling performance at the current density of 5 A g^{-1}.

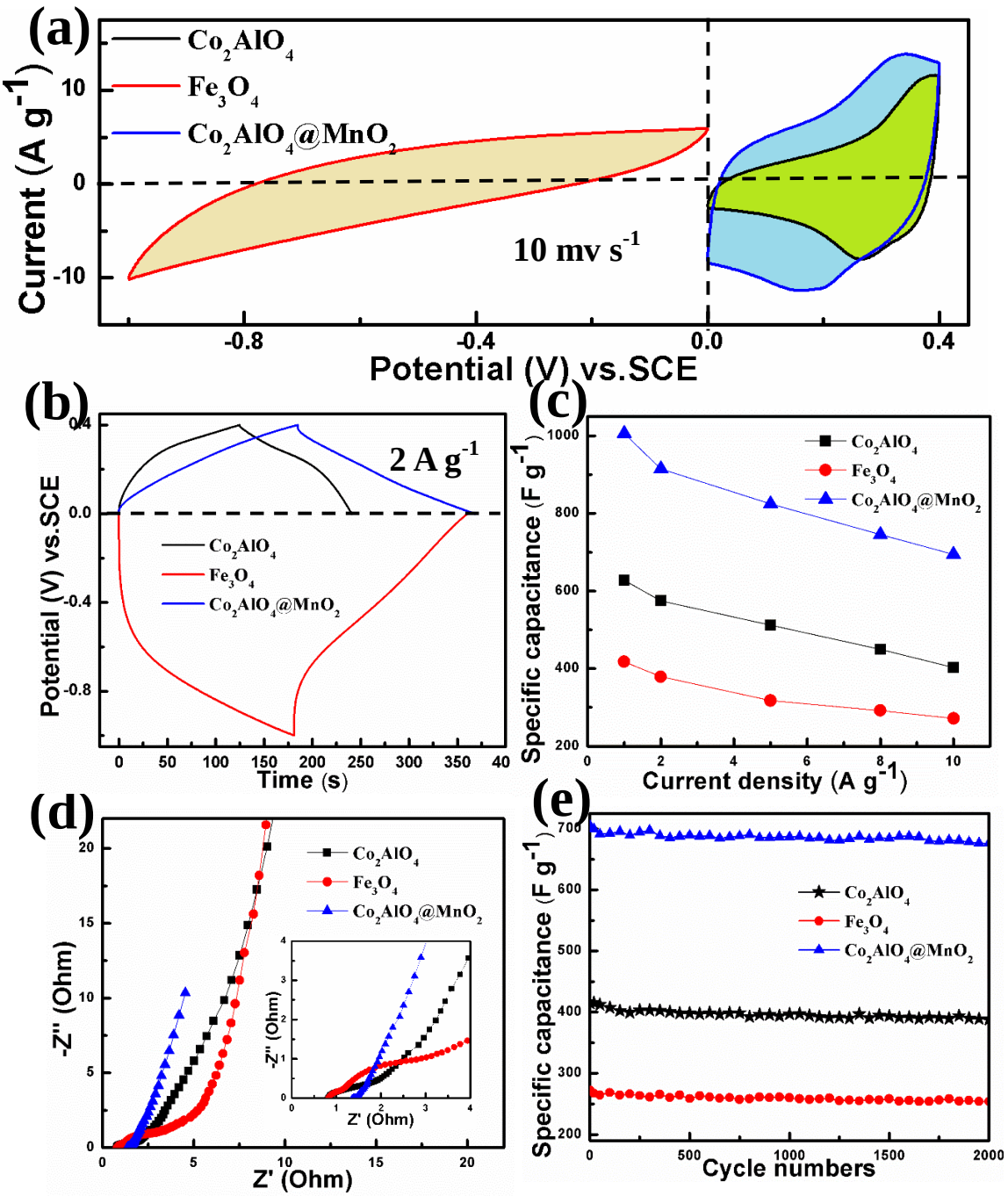

Journal of Materials Chemistry A Accepted Manuscript

Fig. 7. Electrochemical behavior of the NF-Co_2AlO_4@MnO_2// NF-Fe_3O_4 ASC device. (a) Schematic of the full-cell package. (b) CV curves at different scan rates, (c) rate capability, (d) cycling ability with a current of 5 A/g, and (e) Ragone plot of the NF-Co_2AlO_4@MnO_2// NF-Fe_3O_4 ASC device; some values reported from are inserted in (e) for comparison. Insets in (c) are the digital photos of the single electrode and full cell. Insets in (d) are the schematic diagram of the as-assembled NF-Co_2AlO_4@MnO_2// NF-Fe_3O_4 ASC device.

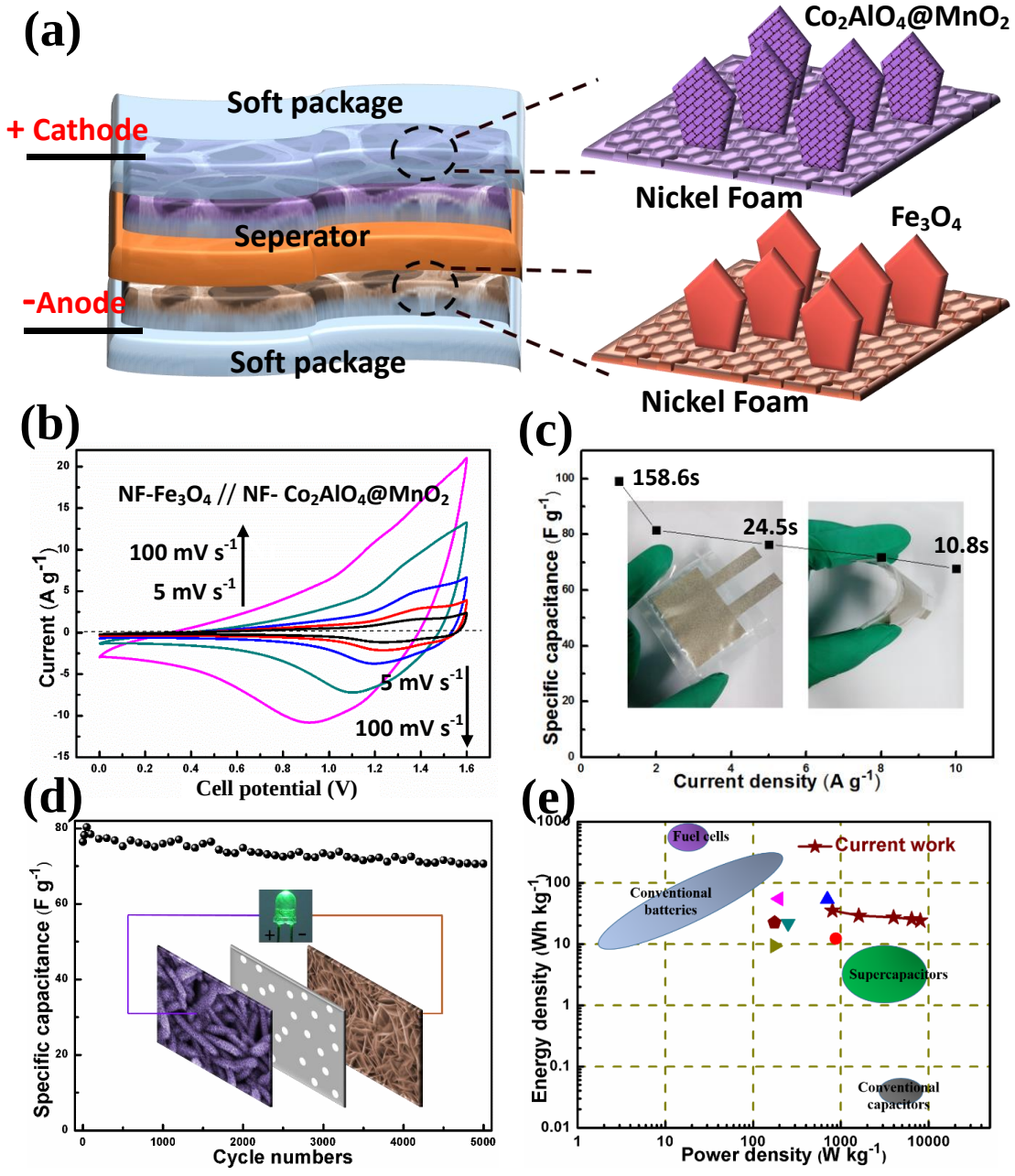

Journal of Materials Chemistry A Accepted Manuscript

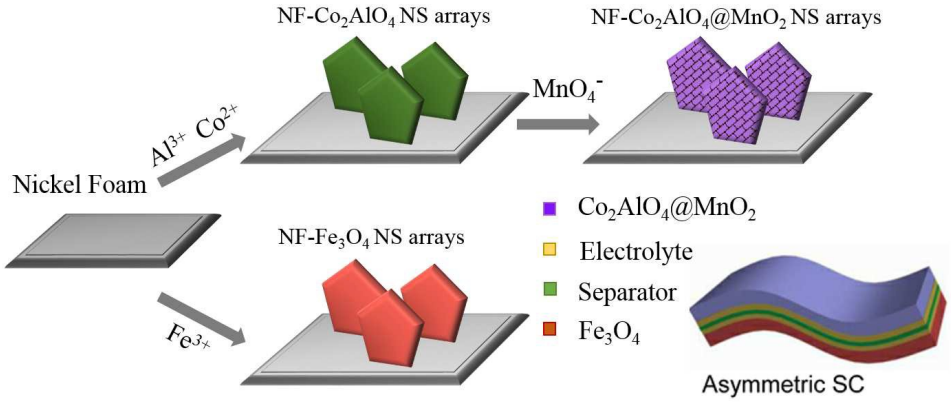

Journal of Materials Chemistry A Accepted Manuscript